Monthly Notices
of the
ROYAL ASTRONOMICAL SOCIETY

MNRAS **442,** 2717–2727 (2014) doi:10.1093/mnras/stu972

Observational rotation curves and density profiles versus the Thomas–Fermi galaxy structure theory

H. J. de Vega,[1,2]★ P. Salucci[3] and N. G. Sanchez[2]

[1]*Sorbonne Universités, UPMC (Univ. Paris VI), CNRS, Laboratoire Associé au CNRS UMR 7589, Tour 13-14, 4ème. et 5ème. étage, Boîte 126, 4, Place Jussieu, F-75252 Paris, France*
[2]*Observatoire de Paris, LERMA, Laboratoire Associé au CNRS UMR 8112, 61, Avenue de l'Observatoire, F-75014 Paris, France*
[3]*SISSA/ISAS and INFN, Trieste, Iniziativa Specifica QSKY, via Bonomea 265, I-34136 Trieste, Italy*

Accepted 2014 May 14. Received 2014 May 12; in original form 2013 November 13

ABSTRACT

The Thomas–Fermi approach to galaxy structure determines self-consistently the gravitational potential of the fermionic warm dark matter (WDM) given its distribution function $f(E)$. This framework is appropriate for macroscopic quantum systems as neutron stars, white dwarfs and WDM galaxies. Compact dwarf galaxies are near the quantum degenerate regime, while large galaxies are in the classical Boltzmann regime. We derive analytic scaling relations for the main galaxy magnitudes: halo radius $r_{\rm h}$, mass $M_{\rm h}$ and phase-space density. Small deviations from the exact scaling show up for compact dwarfs due to quantum macroscopic effects. We contrast the theoretical curves for the circular galaxy velocities $v_{\rm c}(r)$ and density profiles $\rho(r)$ with those obtained from observations using the empirical Burkert profile. Results are independent of any WDM particle physics model, they only follow from the gravitational interaction of the WDM particles and their fermionic nature. The theoretical rotation curves and density profiles reproduce very well the observational curves for $r \lesssim r_{\rm h}$ obtained from 10 different and independent sets of data for galaxy masses from 5×10^9 to $5 \times 10^{11}\,{\rm M}_\odot$. Our normalized theoretical circular velocities and normalized density profiles turn to be universal functions of $r/r_{\rm h}$ for all galaxies. In addition, they agree extremely well with the observational curves described by the Burkert profile for $r \lesssim 2\, r_{\rm h}$. These results show that the Thomas–Fermi approach correctly describes the galaxy structures.

Key words: Galaxy structure – dark matter.

1 INTRODUCTION

Dark matter (DM) is the main component of galaxies: the fraction of DM over the total galaxy mass goes from 95 per cent for large dilute galaxies (Persic, Salucci & Stel 1996; Oh et al. 2008; Memola, Salucci & Babić 2011) to 99.99 per cent for dwarf compact galaxies (Martin, de Jong & Rix 2008; Woo, Courteau & Dekel 2008; Brodie et al. 2011; Willman & Strader 2012; Walker, private communication). Therefore, the study of galaxy properties is an excellent way to disentangle the nature of DM.

Warm dark matter (WDM), which is DM formed by particles with masses in the keV scale, receives increasing attention today (Biermann, de Vega & Sanchez 2012; de Vega, Falvella & Sanchez 2012b; de Vega & Sanchez 2013, and references therein).

At intermediate scales, ∼100 kpc, WDM gives the correct abundance of substructures and therefore WDM solves the cold dark matter (CDM) overabundance of structures at small scales. (Colín, Valenzuela & Avila-Reese 2000; Sommer-Larsen & Dolgov 2001; Gao & Theuns 2007; Tikhonov et al. 2009; Zavala et al. 2009; Papastergis et al. 2011; Lovell et al. 2012, 2014; Anderhalden et al. 2013). For scales larger than 100 kpc, WDM yields the same results as CDM. Hence, WDM agrees with all the observations: small-scale as well as large-scale structure observations and cosmic microwave background (CMB) anisotropy observations.

WDM simulations (as Avila-Reese et al. 2001; Gao & Theuns 2007; Colín., Valenzuela & Avila-Reese 2008; Zavala et al. 2009; Lovell et al. 2012, 2014; Macciò et al. 2012; Viñas, Salvador-Solé & Manrique 2012 and many others) are purely classical (i.e. WDM quantum dynamics is not used in those simulations). The dynamics of DM in the simulations is worked out classically from the classical Newton's equations or self-gravitating hydrodynamics (also classical, without WDM quantum effects). Quantum effects, as the DM quantum pressure, are absent is such frameworks. Inside galaxy cores, below ∼100 pc, WDM *N*-body classical physics simulations do not provide the correct structures because quantum effects are important in WDM at these scales. Classical physics *N*-body WDM simulations without the WDM quantum pressure exhibit cusps or

★ E-mail: devega@lpthe.jussieu.fr

small cores with sizes smaller than the observed cores (Avila-Reese et al. 2001; Colín et al. 2008; Macciò et al. 2012; Viñas et al. 2012). The relevant WDM quantum effect, as discussed in our previous articles (Destri, de Vega & Sanchez 2013a, in what follows DdVS 2013a, Destri, de Vega & Sanchez 2013b, in what follows DdVS 2013b), is the fermionic quantum pressure.

In WDM simulations, the fact that the DM is warm appears in the primordial power spectrum which is suppressed at small scales below the free streaming length. This can be implemented by a simple cutoff or through precise formulas fitting the WDM primordial power spectrum (see Destri, de Vega & Sanchez 2013c for a recent article), and through the non-zero particle velocity dispersion. In addition, in fermionic WDM, the phase-space density is bounded from above by the Pauli principle (DdVS 2013a), see also Tremaine & Gunn (1979). This is the only quantum (fermionic) aspect of WDM implemented in the WDM simulations. Such bound is clearly not enough to account for the quantum pressure of the WDM fermions, because the quantum pressure requires of a combination of both the Pauli principle and the Heisenberg principle. And therefore, the power spectrum cutoff and the Pauli bound on the phase-space density are not enough in the simulations to enlarge the size of the WDM haloes against the gravitation attraction. That is the reason why in WDM simulations the core size problem persists. The presence of a repulsive quantum fermionic pressure is crucial to enlarge enough the haloes against gravitation to account for the macroscopic core sizes. The cutoff in the primordial power spectrum in the WDM simulations is enough to account for the right number of substructures and solve the CDM overabundance problem.

Besides of the cutoff in the primordial power spectrum and the Pauli bound in the phase-space density implemented in the WDM simulations, the crucial point is that in WDM simulations the N-body self-gravitating classical evolution follows the classical Newton's equations. This dynamics in the inner dense regions is far away from the quantum evolution according to the N-body Schrödinger equation and does not contain the quantum fermionic pressure. Instead, the Thomas–Fermi approach corresponds to the Schrödinger equation in the large N regime and contains from the start the quantum pressure. This is the reason why the quantum pressure is naturally contained in the Thomas–Fermi approach and it is not included so far in the classical N-body WDM simulations.

The quantum pressure is well captured in the Thomas–Fermi approach (DdVS 2013a,b). The lack of quantum pressure in the WDM simulations explains why they exhibit cusps or small cores with sizes smaller than the observed cores (Macciò et al. 2012). WDM predicts correct structures and cores with the right sizes for small scales (below the kpc scale) when its quantum nature is taken into account (DdVS 2013a,b).

The quantum effects of matter in the inner halo regions arise because of the quantum fermionic nature and of the quantum uncertainty principle, the combined action of both translates into a non-zero quantum pressure. For macroscopic systems with a large number of particles as galaxies, this translates into macroscopic quantum effects. (Other examples in nature are He^3, white dwarf stars and neutron stars.) The quantum pressure goes as the mass of the particle to the power $-8/3$ and it is therefore much smaller for baryons than for WDM (DdVS 2013a).

The Thomas–Fermi DdVS approach applies irrespective of the WDM particle physics model. The lower bound for the WDM particle mass $m > 1.91$ keV is derived in the Thomas–Fermi approach (DdVS 2013b) from the lightest known dwarf galaxies. This value is independent of the WDM particle physics model.

The main fermionic WDM particle candidate is a sterile neutrino in the keV scale. Many models of sterile neutrinos are available by now (see, for a recent review, Merle 2013). Another fermionic WDM particle candidate is a gravitino in the keV scale.

In summary, all the small-structure formation constraints on the WDM particle mass (Zavala et al. 2009; Papastergis et al. 2011; Lovell et al. 2012, 2014; Menci, Fiore & Lamastra 2013; Nierenberg et al. 2013; Pacucci, Mesinger & Haiman 2013), as well as the bounds from sterile neutrino decay into X-rays (Watson, Li & Polley 2012) favours a WDM particle mass approximately in the 2–3 keV range.

Bounds on the WDM particle mass from Lyman α forest data (Viel et al. 2013) may be not so reliable since they are affected by the difficult-to-characterize non-linear growth of baryonic and DM structures (Watson et al. 2012). Besides these systematic effects from the Lyman α data, there are uncertainities in the WDM simulations themselves, mainly originating from the uncertainty on the chosen initial velocity dispersion for the particles in the simulations whose effective mass is about $10^5\,\mathrm{M}_\odot = 10^{68}$ keV each, as discussed by several authors (Lovell et al. 2012, 2014; Macciò et al. 2012; Viel et al. 2013). Namely the effective particles in the WDM simulations are about 10^{68} times heavier than the real WDM particles. This makes difficult to infer the initial velocity distribution of the effective particles from the known initial velocity distribution of the real WDM particles.

The Lyman α mass bounds are usually given for the thermal relic mass. This is the mass of the WDM particle if it decouples in thermal equilibrium, which is normally not the case for sterile neutrinos. The relation between the physical particle mass and the thermal mass has to be worked out explicitly for each specific particle physics model. About 100 sterile neutrino models are available today (Merle 2013) for which the Lyman α bounds are not known. Therefore, it is not possible so far to provide precise generic Lyman α bounds on the WDM sterile neutrino mass. At present, Lyman α bounds on the WDM particle mass are only available for a few specific particle physics models. For discussions on small-structure formation in WDM and Lyman α bounds on the WDM particle mass, see de Vega et al. (2012b) and Biermann et al. (2012).

The results presented in this paper do not depend on the precise value of the WDM particle mass m but only on the fact that m is in the keV scale.

One can determine the keV scale of the DM particle mass m but not its precise value within the keV scale just from the core radius value of dilute galaxies, those with $M_\mathrm{h} > 10^6\,\mathrm{M}_\odot$ used in this paper.

The aim of this paper is to show that the obtained rotation curves and density profiles in the Thomas–Fermi galaxy structure theory are in well agreement with the galaxy data parametrized with Burkert profiles.

We follow here the Thomas–Fermi approach to galaxy structure for self-gravitating fermionic WDM (DdVS 2013a,b). This approach is especially appropriate to take into account quantum properties of systems with large number of particles, that is, macroscopic quantum systems as neutron stars and white dwarfs (Landau & Lifshits 1980). In this approach, the central quantity to derive is the DM chemical potential $\mu(\boldsymbol{r})$, which is the free energy per particle. For self-gravitating systems, the potential $\mu(\boldsymbol{r})$ is proportional to the gravitational potential $\phi(\boldsymbol{r})$,

$$\mu(\boldsymbol{r}) = \mu_0 - m\,\phi(\boldsymbol{r})\,, \tag{1}$$

μ_0 being a constant, and obeys the self-consistent and non-linear Poisson equation

$$\nabla^2\mu(\boldsymbol{r}) = -4\,\pi\,g\,G\,m^2\,\int \frac{\mathrm{d}^3p}{(2\,\pi\,\hbar)^3}\,f\left(\frac{p^2}{2\,m}-\mu(\boldsymbol{r})\right). \qquad (2)$$

Here, G is Newton's gravitational constant, g is the number of internal degrees of freedom of the DM particle, p is the DM particle momentum and $f(E)$ is the energy distribution function. This is a semiclassical gravitational approach to determine self-consistently the gravitational potential of the fermionic WDM given its distribution function $f(E)$.

In the Thomas–Fermi approach, DM-dominated galaxies are considered in a stationary state. This is a realistic situation for the late stages of structure formation since the free-fall (Jeans) time $t_{\rm ff}$ for galaxies is much shorter than the age of galaxies. $t_{\rm ff}$ is at least one or two orders of magnitude smaller than the age of the galaxy.

We consider spherical symmetric configurations where equation (2) becomes an ordinary non-linear differential equation that determines self-consistently the chemical potential $\mu(r)$ and constitutes the Thomas–Fermi approach (DdVS 2013a,b). We choose for the energy distribution function a Fermi–Dirac distribution

$$f(E) = \frac{1}{\mathrm{e}^{E/E_0}+1}\,,$$

where E_0 is the characteristic one-particle energy scale. E_0 plays the role of an effective temperature scale and depends on the galaxy mass. The Fermi–Dirac distribution function is justified in the inner regions of the galaxy, inside the halo radius where we find that the Thomas–Fermi density profiles perfectly agree with the observational data modelized with the empirical Burkert profile.

Observations show that the DM angular momentum is small. In spirals, we have a direct proof of this fact from their bottom-up general scenario of formation. In these objects, we can compute from observations the disc angular momentum; if the angular momentum per unit mass is conserved during the process of disc formation, the values found imply that DM haloes are not dominated by rotation (Tonini et al. 2006). Therefore, the spherical symmetric approximation makes sense. Indeed, our results confirm the consistency of such assumption.

In this paper, spherical symmetry is considered for simplicity to determine the essential physical galaxy properties as the classical or quantum nature of galaxies, compact or dilute galaxies, the phase-space density values, the cored nature of the mass density profiles, the galaxy masses and sizes. It is clear that DM haloes are not perfectly spherical but describing them as spherically symmetric is a first approximation to which other effects can be added. In DdVS (2013a), we estimated the angular momentum effect and this yields small corrections.

Our spherically symmetric treatment captures the essential features of the gravitational dynamics and agrees with the observations. Note that we are treating the DM particles quantum mechanically through the Thomas–Fermi approach, so that expectation values are independent of the angles (spherical symmetry) but the particles move and fluctuate in all directions in totally non-spherically symmetric ways. Namely this is more than treating purely classical orbits for particles in which only radial motion is present. The Thomas–Fermi approach to galaxies can be generalized to describe non-spherically symmetric and non-isotropic situations, by considering distribution functions which include other particle parameters like the angular momentum.

The solutions of the Thomas–Fermi equation (2) are characterized by the value of the chemical potential at the origin $\mu(0)$. Large positive values of $\mu(0)$ correspond to dwarf compact galaxies (fermions near the quantum degenerate limit), while large negative values of $\mu(0)$ yield large and dilute galaxies (classical Boltzmann regime).

Approaching the classical diluted limit yields larger and larger halo radii, galaxy masses and velocity dispersions. In contrast, in the quantum degenerate limit, we get solutions of the Thomas–Fermi equations corresponding to the minimal halo radii, galaxy masses and velocity dispersions.

The surface density

$$\Sigma_0 \equiv r_{\rm h}\,\rho_0 \simeq 120\ \mathrm{M}_\odot\,\mathrm{pc}^{-2} \quad \text{up to 10–20 per cent} \qquad (3)$$

has the remarkable property of being nearly constant and independent of luminosity in different galactic systems (spirals, dwarf irregular and spheroidals, ellipticals) spanning over 14 mag in luminosity and over different Hubble types (Spano et al. 2008; Donato et al. 2009). It is therefore a useful characteristic scale to express galaxy magnitudes.

To reproduce the smaller observed structures, the WDM particle mass should be in the keV scale. We choose the value 2 keV as references scale to express physical magnitudes.

In this paper, we compute the circular velocity in the Thomas–Fermi approach using its expression in terms of the chemical potential:

$$v_{\rm c}(r) = \sqrt{\frac{G\,M(r)}{r}} = \sqrt{-\frac{r}{m}\,\frac{\mathrm{d}\mu}{\mathrm{d}r}}\,.$$

On the other hand, the circular velocities of galaxies are known with precision from the observational data from the kinematics of thousands of disc galaxies and from the information arising from other tracers of the gravitational field of galaxies as the dispersion velocities of spheroidals and weak-lensing measurements (Salucci et al. 2007, and references therein). All this evidence shows that an empirical Burkert profile (Donato et al. 2009)

$$\rho_{\rm B}(r) = \frac{\rho_0}{\left(1+\frac{r}{r_{\rm h}}\right)\left[1+\left(\frac{r}{r_{\rm h}}\right)^2\right]} \qquad (4)$$

correctly reproduces the observations out to the galaxy virial radius. The two parameters in the Burkert profile, ρ_0 and $r_{\rm h}$ are defined by $\rho_{\rm B}(0) \equiv \rho_0$ and $\rho_{\rm B}(r_{\rm h}) \equiv \rho_0/4$.

In this paper, we contrast the observational curves for the circular velocities of galaxies $V_{\rm URC,h}(r)$ and the density profiles obtained from observations using the empirical Burkert profile (equation 4) with the theoretical results $v_{\rm c}(r)$ and $\rho(r)$ arising from the resolution of the Thomas–Fermi equations.

Our theoretical results follow solving the self-consistent and non-linear Poisson equation (equation 2) which is solely derived from the purely gravitational interaction of the WDM particles and their fermionic nature. All results are valid for self-gravitating fermionic WDM particles which are assumed stable (or with a lifetime of the order or longer than the Hubble time). The non-gravitational interactions of the WDM particles are assumed weak enough to satisfy the particle accelerator bounds and beta decay bounds. Except for these general WDM particle properties, the framework described here does not require any particular particle physics model of WDM production. All the results reported here are independent of the details of the WDM particle physics model as the symmetry group and the values of the weak enough particle couplings.

The theoretical rotation curves and density profiles well reproduce inside the halo radius the observational curves described by the

empirical Burkert profile, obtained from 10 different and independent sets of data for galaxy masses from 5×10^9 to $5 \times 10^{11}\,\mathrm{M}_\odot$.

Our theoretical circular velocities and density profiles exhibit the universal property as the observational curves do, and in addition, they coincide with the observational curves described by the empirical Burkert profile for $r \lesssim 2\, r_\mathrm{h}$.

In summary, the results presented in this paper show the ability of the Thomas–Fermi approach to correctly describe the galaxy structures.

This paper is organized as follows. In Section 2, we present the Thomas–Fermi approach to galaxy structure and we express the main galaxy magnitudes in terms of the solution of the Thomas–Fermi equation and the value of the surface density Σ_0. We discuss the theoretical circular velocity curves, the theoretical density profiles and the remarkable universality of them. In Section 3, we present the contrast between the observational and theoretical curves for the galaxy circular velocities and the density profiles and we discuss the universal property of these profiles. Section 4 is devoted to our conclusions.

2 GALAXY PROPERTIES IN THE THOMAS–FERMI WDM APPROACH

We consider DM-dominated galaxies in their late stages of structure formation when they are relaxing to a stationary situation, at least not too far from the galaxy centre.

This is a realistic situation since the free-fall (Jeans) time t_ff for galaxies is much shorter than the age of galaxies:

$$t_\mathrm{ff} = \frac{1}{\sqrt{G\,\rho_0}} = 1.49 \times 10^7 \sqrt{\frac{\mathrm{M}_\odot}{\rho_0\ \mathrm{pc}^3}}\ \mathrm{yr}\ .$$

The observed central densities of galaxies yield free-fall times in the range from 15 million years for ultracompact galaxies to 330 million years for large dilute spiral galaxies. These free-fall (or collapse) times are small compared with the age of galaxies running in billions of years.

Hence, we can consider the DM described by a time-independent and non-relativistic energy distribution function $f(E)$, where $E = p^2/(2m) - \mu$ is the single-particle energy, m is the mass of the DM particle, μ is the chemical potential (DdVS 2013a,b) related to the gravitational potential $\phi(\boldsymbol{r})$ by equation (1).

In the Thomas–Fermi approach, $\rho(\boldsymbol{r})$ is expressed as a function of $\mu(\boldsymbol{r})$ through the standard integral of the DM phase-space distribution function over the momentum

$$\rho(\boldsymbol{r}) = \frac{g\,m}{2\,\pi^2\,\hbar^3}\int_0^\infty \mathrm{d}p\ p^2\ f\left(\frac{p^2}{2m} - \mu(\boldsymbol{r})\right), \tag{5}$$

where g is the number of internal degrees of freedom of the DM particle, with $g = 1$ for Majorana fermions and $g = 2$ for Dirac fermions. For definiteness, we will take $g = 2$ in the sequel.

We will consider spherical symmetric configurations. Then, the Poisson equation for $\phi(r)$ takes the self-consistent form

$$\frac{\mathrm{d}^2\mu}{\mathrm{d}r^2} + \frac{2}{r}\,\frac{\mathrm{d}\mu}{\mathrm{d}r} = -4\pi\,G\,m\,\rho(r) = -\frac{4\,G\,m^2}{\pi\,\hbar^3}\int_0^\infty \mathrm{d}p\ p^2\ f\left(\frac{p^2}{2m} - \mu(r)\right), \tag{6}$$

where G is Newton's constant and $\rho(r)$ is the DM mass density.

Equation (6) provides an ordinary non-linear differential equation that determines self-consistently the chemical potential $\mu(r)$ and constitutes the Thomas–Fermi approach (DdVS 2013a,b). This is a semiclassical approach to galaxy structure in which the quantum nature of the DM particles is taken into account through the quantum statistical distribution function $f(E)$.

The DM pressure and the velocity dispersion can also be expressed as integrals over the DM phase-space distribution function as

$$P(r) = \frac{1}{3\,\pi^2\,m\,\hbar^3}\int_0^\infty \mathrm{d}p\ p^4\ f\left(\frac{p^2}{2m} - \mu(r)\right),$$

$$\langle v^2\rangle(r) = \frac{1}{m^2}\,\frac{\int_0^\infty \mathrm{d}p\ p^4\ f\left(\frac{p^2}{2m} - \mu(r)\right)}{\int_0^\infty \mathrm{d}p\ p^2\ f\left(\frac{p^2}{2m} - \mu(r)\right)} = 3\,\frac{P(r)}{\rho(r)}\ . \tag{7}$$

The fermionic DM mass density ρ is bounded at the origin due to the Pauli principle (DdVS 2013a) which implies the bounded boundary condition at the origin as

$$\frac{\mathrm{d}\mu}{\mathrm{d}r}(0) = 0\ . \tag{8}$$

We see that $\mu(r)$ fully characterizes the DM halo structure in this Thomas–Fermi framework. The chemical potential is monotonically decreasing in r since equation (6) implies

$$\frac{\mathrm{d}\mu}{\mathrm{d}r} = -\frac{G\,m\,M(r)}{r^2}, \qquad M(r) = 4\pi\int_0^r \mathrm{d}r'\,r'^2\,\rho(r')\ . \tag{9}$$

In this semiclassical framework, the stationary energy distribution function $f(E)$ must be given. We consider the Fermi–Dirac distribution

$$f(E) = \Psi_\mathrm{FD}(E/E_0) = \frac{1}{\mathrm{e}^{E/E_0} + 1}\ , \tag{10}$$

where the characteristic one-particle energy scale E_0 in the DM halo plays the role of an effective temperature. The value of E_0 depends on the galaxy mass. In neutron stars, where the neutron mass is about six orders of magnitude larger than the WDM particle mass, the temperature can be approximated by zero. In galaxies, $E_0 \sim m\,\langle v^2\rangle$ turns to be non-zero but small in the range $10^{-3}\ \mathrm{K} \lesssim E_0 \lesssim 50\ \mathrm{K}$ which reproduce the observed velocity dispersions for $m \sim 2$ keV. The smaller values of E_0 correspond to compact dwarf galaxies and the larger values of E_0 are for large and dilute galaxies.

Note that for the relevant galaxy physical magnitudes, the Fermi–Dirac distribution function gives similar results to out-of-equilibrium distribution functions (DdVS 2013a).

The choice of Ψ_FD is justified in the inner regions, where relaxation to thermal equilibrium is possible. Far from the origin, however, the Fermi–Dirac distribution as its classical counterpart, the isothermal sphere, produces a mass density tail $1/r^2$ that overestimates the observed tails of the galaxy mass densities. Indeed, the classical regime $\mu/E_0 \to -\infty$ is attained for large distances r since equation (9) indicates that $\mu(r)$ is always monotonically decreasing with r.

More precisely, large positive values of the chemical potential at the origin correspond to the degenerate fermions limit which is the extreme quantum case and oppositely, large negative values of the chemical potential at the origin gives the diluted case which is the classical regime. The quantum degenerate regime describes dwarf and compact galaxies while the classical and diluted regime describes large and diluted galaxies. In the classical regime, the Thomas–Fermi equations (6)–(8) become the equations for a self-gravitating Boltzmann gas.

It is useful to introduce dimensionless variables $\xi, \nu(\xi)$

$$r = l_0\,\xi, \qquad \mu(r) = E_0\,\nu(\xi), \tag{11}$$

where l_0 is the characteristic length that emerges from the dynamical equation (6):

$$l_0 \equiv \frac{\hbar}{\sqrt{8\,G}}\left[\frac{9\,\pi\,I_2(\nu_0)}{m^8\,\rho_0}\right]^{1/6} = R_0\,\left(\frac{2\,\mathrm{keV}}{m}\right)^{4/3}\left[\frac{I_2(\nu_0)}{\rho_0}\,\frac{\mathrm{M}_\odot}{\mathrm{pc}^3}\right]^{1/6},$$
$$R_0 = 7.425\ \mathrm{pc}, \tag{12}$$

and

$$I_n(\nu) \equiv (n+1)\int_0^\infty y^n\,\mathrm{d}y\,\Psi_{\mathrm{FD}}(y^2-\nu),$$
$$n = 1, 2, \ldots, \quad \nu_0 \equiv \nu(0), \quad \rho_0 = \rho(0), \tag{13}$$

where we use the integration variable $y \equiv p/\sqrt{2\,m\,E_0}$.

Then, in dimensionless variables, the self-consistent Thomas–Fermi equation (6) for the chemical potential $\nu(\xi)$ takes the form

$$\frac{\mathrm{d}^2\nu}{\mathrm{d}\xi^2} + \frac{2}{\xi}\,\frac{\mathrm{d}\nu}{\mathrm{d}\xi} = -I_2(\nu), \quad \nu'(0) = 0. \tag{14}$$

We solve equation (14) numerically by using as independent variable $u \equiv \ln\xi$ and then applying the fourth-order Runge–Kutta method. We solve equation (14) for a broad range of values $\nu_0 \equiv \nu(0)$, from negative values $\nu_0 \lesssim -5$ describing galaxies in dilute regimes to positive values $\nu_0 \gtrsim 1$ corresponding to compact dwarf galaxies.

We find the main physical galaxy magnitudes, such as the mass density $\rho(r)$, the velocity dispersion $\sigma^2(r) = v^2(r)/3$ and the pressure $P(r)$, which are all r-dependent as

$$\rho(r) = \rho_0\,\frac{I_2(\nu(\xi))}{I_2(\nu_0)}, \quad \rho_0 = \frac{1}{3\,\pi^2}\,\frac{m^4}{\hbar^3}\left(\frac{2\,E_0}{m}\right)^{3/2} I_2(\nu_0)\,,$$
$$\sigma(r) = \sqrt{\frac{2\,E_0}{5\,m}\,\frac{I_4(\nu(\xi))}{I_2(\nu(\xi))}} \tag{15}$$
$$= 1.092\,\sqrt{\frac{I_4(\nu(\xi))}{I_2(\nu(\xi))}}\,\left(\frac{2\,\mathrm{keV}}{m}\right)^{4/3}\left[\frac{\rho_0}{I_2(\nu_0)}\,\frac{\mathrm{pc}^3}{\mathrm{M}_\odot}\right]^{1/3}\mathrm{km\,s^{-1}}, \tag{16}$$

$$P(r) = \frac{2\,E_0}{5\,m}\,\rho_0\,\frac{I_4(\nu(\xi))}{I_2(\nu_0)}$$
$$= \frac{1}{5}\,\left(\frac{3\,\pi^2\,\hbar^3}{m^4}\right)^{2/3}\left[\frac{\rho_0}{I_2(\nu_0)}\right]^{5/3} I_4(\nu(\xi))\,. \tag{17}$$

As a consequence, from equations (9), (11), (12), (14) and (15), the total mass $M(r)$ enclosed in a sphere of radius r and the phase-space density $Q(r)$ turn to be

$$M(r) = 4\,\pi\,\frac{\rho_0\,l_0^3}{I_2(\nu_0)}\int_0^\xi \mathrm{d}x\,x^2\,I_2(\nu(x))$$
$$= 4\,\pi\,\frac{\rho_0\,l_0^3}{I_2(\nu_0)}\,\xi^2\,|\nu'(\xi)|$$
$$= M_0\,\xi^2\,|\nu'(\xi)|\,\left(\frac{\mathrm{keV}}{m}\right)^4\,\sqrt{\frac{\rho_0}{I_2(\nu_0)}\,\frac{\mathrm{pc}^3}{\mathrm{M}_\odot}}\,,$$

$$M_0 = 4\,\pi\,\mathrm{M}_\odot\,\left(\frac{R_0}{\mathrm{pc}}\right)^3 = 0.8230\times10^5\,\mathrm{M}_\odot\,, \tag{18}$$

$$Q(r) \equiv \frac{\rho(r)}{\sigma^3(r)} = 3\,\sqrt{3}\,\frac{\rho(r)}{\langle v^2\rangle^{3/2}(r)}$$
$$= \frac{\sqrt{125}}{3\,\pi^2}\,\frac{m^4}{\hbar^3}\,\frac{I_2^{5/2}(\nu(\xi))}{I_4^{3/2}(\nu(\xi))}\,. \tag{19}$$

We have systematically eliminated the energy scale E_0 in terms of the central density ρ_0 through equation (15). Note that $Q(r)$ turns to be independent of E_0 and therefore from ρ_0.

We define the core size r_h of the halo by analogy with the empirical Burkert density profile as

$$\frac{\rho(r_\mathrm{h})}{\rho_0} = \frac{1}{4}, \quad r_\mathrm{h} = l_0\,\xi_\mathrm{h}. \tag{20}$$

It must be noticed that the surface density,

$$\Sigma_0 \equiv r_\mathrm{h}\,\rho_0, \tag{21}$$

is found nearly constant and independent of luminosity in different galactic systems (spirals, dwarf irregular and spheroidals, elliptics) spanning over 14 mag in luminosity and over different Hubble types. More precisely, all galaxies seem to have the same value for Σ_0, namely $\Sigma_0 \simeq 120\,\mathrm{M}_\odot\,\mathrm{pc}^{-2}$ up to 10–20 per cent (Kormendy & Freeman 2004; Spano et al. 2008; Donato et al. 2009). It is remarkable that at the same time other important structural quantities as r_h, ρ_0, the baryon fraction and the galaxy mass vary orders of magnitude from one galaxy to another.

The constancy of Σ_0 seems unlikely to be a mere coincidence and probably reflects a physical scaling relation between the mass and halo size of galaxies. It must be stressed that Σ_0 is the only dimensionful quantity which is constant among the different galaxies.

We use here the dimensionful quantity Σ_0 to set the energy scale in the Thomas–Fermi approach. That is, we replace the central density ρ_0 in equations (11), (12), (15) and (18) in terms of Σ_0 (equation 21) with the following results:

$$l_0 = \frac{\hbar^{6/5}}{G^{3/5}}\,\left(\frac{9\,\pi}{512}\right)^{1/5}\,\left[\frac{\xi_\mathrm{h}\,I_2(\nu_0)}{m^8\,\Sigma_0}\right]^{1/5}$$
$$= 4.2557\,\left[\xi_\mathrm{h}\,I_2(\nu_0)\right]^{1/5}\,\left(\frac{2\,\mathrm{keV}}{m}\right)^{8/5}\,\left(\frac{120\,\mathrm{M}_\odot}{\Sigma_0\,\mathrm{pc}^2}\right)^{1/5}\,\mathrm{pc}\,,$$

$$E_0 = \hbar^{6/5}\,\frac{G^{2/5}}{m^{3/5}}\,\left(18\,\pi^6\right)^{1/5}\,\left[\frac{\Sigma_0}{\xi_\mathrm{h}\,I_2(\nu_0)}\right]^{4/5}$$
$$= \frac{7.127\,57\times10^{-3}}{\left[\xi_\mathrm{h}\,I_2(\nu_0)\right]^{4/5}}\,\left(\frac{2\,\mathrm{keV}}{m}\right)^{3/5}\,\left(\frac{\Sigma_0\,\mathrm{pc}^2}{120\,\mathrm{M}_\odot}\right)^{4/5}\,\mathrm{K}, \tag{22}$$

and

$$r = 4.2557\,\xi\,\left[\xi_\mathrm{h}\,I_2(\nu_0)\right]^{1/5}\,\left(\frac{2\,\mathrm{keV}}{m}\right)^{8/5}\,\left(\frac{120\,\mathrm{M}_\odot}{\Sigma_0\,\mathrm{pc}^2}\right)^{1/5}\,\mathrm{pc}, \tag{23}$$

$$\rho(r) = 18.1967\,\frac{I_2(\nu(\xi))}{\left[\xi_\mathrm{h}\,I_2(\nu_0)\right]^{6/5}}\,\left(\frac{m}{2\,\mathrm{keV}}\right)^{8/5}\,\left(\frac{120\,\mathrm{M}_\odot}{\Sigma_0\,\mathrm{pc}^2}\right)^{6/5}\,\frac{\mathrm{M}_\odot}{\mathrm{pc}^3},$$
$$M(r) = \frac{27\,312\xi^2}{\left[\xi_\mathrm{h}\,I_2(\nu_0)\right]^{3/5}}|\nu'(\xi)|\,\left(\frac{2\,\mathrm{keV}}{m}\right)^{16/5}\,\left(\frac{\Sigma_0\mathrm{pc}^2}{120\mathrm{M}_\odot}\right)^{3/5}\,\mathrm{M}_\odot. \tag{24}$$

For a fixed value of the surface density Σ_0, the solutions of the Thomas–Fermi equation (14) are parametrized by a single

parameter: the dimensionless chemical potential at the centre ν_0. That is, ν_0 is determined by the value of the halo galaxy mass

$$M_{\rm h} \equiv M(r_{\rm h}). \tag{25}$$

In the classical dilute limit, $\nu_0 \lesssim -5$, the analytic expressions for the main galaxies magnitudes are given by

$$\xi_{\rm h} = \frac{3.147\,473}{e^{\nu_0/2}}, \quad \left.\frac{d\nu}{d\ln\xi}\right|_{\xi_{\rm h}} = -1.839\,957, \tag{26}$$

$$M_{\rm h} = 1.755\,72\ \Sigma_0\ r_{\rm h}^2,$$

$$M_{\rm h} = \frac{67\,011.4}{e^{\frac{4}{5}\nu_0}} \left(\frac{2\,{\rm keV}}{m}\right)^{16/5} \left(\frac{\Sigma_0\ {\rm pc}^2}{120\ {\rm M}_\odot}\right)^{3/5} {\rm M}_\odot,$$

$$r_{\rm h} = 68.894 \sqrt{\frac{M_{\rm h}}{10^6\ {\rm M}_\odot}} \sqrt{\frac{120\ {\rm M}_\odot}{\Sigma_0\ {\rm pc}^2}}\ {\rm pc}, \tag{27}$$

$$r = 22.728\ \xi \left(\frac{{\rm M}_\odot}{M_{\rm h}}\right)^{1/8} \left(\frac{2\,{\rm keV}}{m}\right)^{2} \left(\frac{120\ {\rm M}_\odot}{\Sigma_0\ {\rm pc}^2}\right)^{1/8} {\rm pc}, \tag{28}$$

$$\rho(r) = 5.195\,045 \left(\frac{M_{\rm h}}{10^4\ {\rm M}_\odot}\right)^{3/4} \left(\frac{m}{2\,{\rm keV}}\right)^{4} \left(\frac{\Sigma_0\ {\rm pc}^2}{120\ {\rm M}_\odot}\right)^{3/4} \times e^{\nu(\xi)}\ \frac{{\rm M}_\odot}{{\rm pc}^3}, \tag{29}$$

$$M(r) = 179.30 \left(\frac{M_{\rm h}}{{\rm M}_\odot}\right)^{3/4} \left(\frac{2\,{\rm keV}}{m}\right)^{2} \left(\frac{\Sigma_0\ {\rm pc}^2}{120\ {\rm M}_\odot}\right)^{3/8} \times \xi \left|\frac{d\nu(\xi)}{d\ln\xi}\right| {\rm M}_\odot, \tag{30}$$

$$Q(0) = 1.2319 \left(\frac{10^5\ {\rm M}_\odot}{M_{\rm h}}\right)^{5/4} \left(\frac{\Sigma_0\ {\rm pc}^2}{120\ {\rm M}_\odot}\right)^{3/4} {\rm keV}^4. \tag{31}$$

These equations are accurate for $M_{\rm h} \gtrsim 10^6\ {\rm M}_\odot$. We see that they exhibit a scaling behaviour for $r_{\rm h}$ versus $M_{\rm h}$, $Q_{\rm h}$ and $Q(0)$ versus $M_{\rm h}$ and $M_{\rm h}$ versus the fugacity at the centre $z_0 = e^{\nu_0}$. These scaling behaviours are very accurate except near the degenerate limit as shown by Fig. 1.

It must be stressed that (i) the scaling relations (equations 26–31) are a consequence solely of the self-gravitating interaction of the fermionic WDM and (ii) the value of the WDM particle mass $m \simeq 2$ keV appears in the proportionality factors.

We plot in Fig. 1 the ordinary logarithm of

$$\hat{r}_{\rm h} \equiv \frac{r_{\rm h}}{\rm pc} \left(\frac{m}{2\,{\rm keV}}\right)^{8/5} \left(\frac{\Sigma_0\ {\rm pc}^2}{120\ {\rm M}_\odot}\right)^{1/5} \tag{32}$$

versus the ordinary logarithm of

$$\hat{M}_{\rm h} \equiv \frac{M_{\rm h}}{{\rm M}_\odot} \left(\frac{m}{2\,{\rm keV}}\right)^{16/5} \left(\frac{120\ {\rm M}_\odot}{\Sigma_0\ {\rm pc}^2}\right)^{3/5}. \tag{33}$$

From equations (26), (32) and (33), we find the scaling relation

$$\log_{10}\hat{r}_{\rm h} = \frac{1}{2}\ \log_{10}\hat{M}_{\rm h} - 1.161\,82\ , \tag{34}$$

which is accurate for $M_{\rm h} \gtrsim 10^6\ {\rm M}_\odot$.

Actually, the dilute regime formulas (equations 26–31) apply even near the fermion degenerate limit as shown by Fig. 1. In

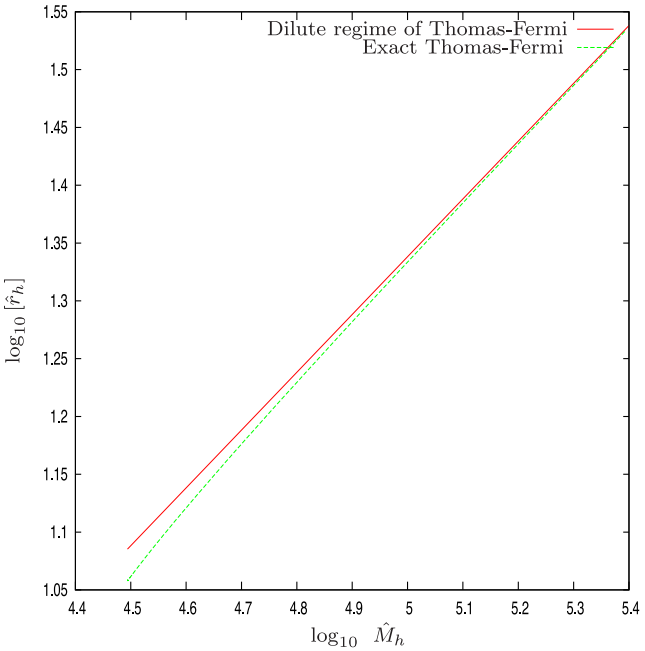

Figure 1. The ordinary logarithm of the theoretical halo radius $\hat{r}_{\rm h}$ versus the ordinary logarithm of the halo mass $\hat{M}_{\rm h}$ for small galaxy masses in the Thomas–Fermi approach from equations (20), (24), (25), (32) and (33) (dashed green line) and the dilute regime equations (26) and (27) (red continuous line). $\hat{r}_{\rm h}$ and $\hat{M}_{\rm h}$ are defined by equations (32) and (33). The dilute regime approximates very well the exact Thomas–Fermi results, $r_{\rm h}$ follows the square-root of $M_{\rm h}$ scaling behaviour of the classical regime (equations 26 and 27). This is so even near the fermion degenerate quantum limit.

Fig. 1, we depicted $\log_{10}\hat{r}_{\rm h}$ versus $\log_{10}\hat{M}_{\rm h}$ for the smaller galaxies $\hat{M}_{\rm h,min} \le \hat{M}_{\rm h} < 10^5$ where $\hat{M}_{\rm h,min} = 30\,999$. We see that the dilute regime equations (26)–(31) reproduce the Thomas–Fermi results for practically all galaxy masses even near the degenerate limit.

In equations (23)–(31), we use the surface density Σ_0 as energy scale to express the theoretical results (we used the central density ρ_0 in DdVS 2013a,b). It is highly remarkable that our theoretical results reproduce the observed DM halo properties with good precision.

The opposite limit $\nu_0 \gtrsim 1$ is the extreme quantum limit corresponding to degenerate WDM fermions. The galaxy mass and halo radius take in the degenerate limit their minimum values

$$r_{\rm h}^{\rm min} = 11.3794 \left(\frac{2\,{\rm keV}}{m}\right)^{8/5} \left(\frac{120\ {\rm M}_\odot}{\Sigma_0\ {\rm pc}^2}\right)^{1/5} {\rm pc},$$

$$M_{\rm h}^{\rm min} = 30\,998.7 \left(\frac{2\,{\rm keV}}{m}\right)^{16/5} \left(\frac{\Sigma_0\ {\rm pc}^2}{120\ {\rm M}_\odot}\right)^{3/5} {\rm M}_\odot, \tag{35}$$

while the phase-space density $Q(r)$ takes its maximum value

$$Q_{\rm h}^{\rm max} = 16\frac{\sqrt{125}}{3\,\pi^2} \left(\frac{m}{2\,{\rm keV}}\right)^4 {\rm keV}^4 = 6.041\,628 \left(\frac{m}{2\,{\rm keV}}\right)^4 {\rm keV}^4. \tag{36}$$

But the Thomas–Fermi equations provide a whole continuous range of galaxy solutions above the degenerate limit as discussed above and in DdVS (2013a,b).

The degenerate limit corresponds to $E_0 = 0$. In the classical dilute limit $M_{\rm h} \gtrsim 10^6\ {\rm M}_\odot$, E_0 runs approximately from 0.02 to 20 K.

2.1 The galaxy circular velocities

We consider now the circular velocity $v_c(r)$ defined through the virial theorem as

$$v_c(r) \equiv \sqrt{\frac{G\ M(r)}{r}}\ . \tag{37}$$

The circular velocity is directly related by equation (9) to the derivative of the chemical potential as

$$v_c(r) = \sqrt{-\frac{r}{m}\ \frac{\mathrm{d}\mu}{\mathrm{d}r}},$$

which in dimensionless variables takes the form

$$v_c(r) = \sqrt{-\frac{E_0}{m}\ \frac{\mathrm{d}v}{\mathrm{d}\ln\xi}}.$$

Expressing the energy scale E_0 in terms of the surface density using equation (22), we have for the circular velocity the explicit expression

$$v_c(r) = 5.2537 \frac{\sqrt{-\xi\, \nu'(\xi)}}{[\xi_h I_2(\nu_0)]^{2/5}} \left(\frac{2\,\mathrm{keV}}{m}\right)^{4/5} \left(\frac{\Sigma_0 \mathrm{pc}^2}{120 \mathrm{M}_\odot}\right)^{2/5} \mathrm{km\,s^{-1}}. \tag{38}$$

In the dilute Boltzmann regime, the circular velocity at the core radius r_h scales as the power 1/4 of the galaxy halo mass M_h:

$$v_c(r_h) = 7.901 \left(\frac{M_h}{10^6\ \mathrm{M}_\odot}\right)^{1/4} \left(\frac{\Sigma_0\ \mathrm{pc}^2}{120\ \mathrm{M}_\odot}\right)^{1/4} \mathrm{km\,s^{-1}}. \tag{39}$$

It is important to consider the circular velocity normalized to unit at the core radius r_h

$$U(x) \equiv \frac{v_c(r)}{v_c(r_h)} = \sqrt{x\ \frac{\nu'(\xi)}{\nu'(\xi_h)}}, \quad x = \frac{r}{r_h}. \tag{40}$$

Explicitly solving the Thomas–Fermi equation (14), we find that $v_c(r)/v_c(r_h)$ is only function of $x = r/r_h$ and takes the same values for all galaxy masses in the range going from 5.13×10^9 to $5.15 \times 10^{11}\ \mathrm{M}_\odot$ as shown in Fig. 2. Namely $U(x)$ turns to be a universal function.

This is a remarkable result since a priori $v_c(r)/v_c(r_h)$ could be a function of r and r_h and could be different for different galaxies.

This important result shows the ability of the Thomas–Fermi approach to correctly describe the galaxy structures.

The phase-space density $Q(r)$ can be also obtained from the circular velocity at the radius r as

$$Q_c(r) = 3\sqrt{3}\ \frac{\rho(r)}{v_c^3(r)}, \quad Q_{ch} = 3\sqrt{3}\ \frac{\rho(r_h)}{v_c^3(r_h)}. \tag{41}$$

Expressing $\rho(r_h)$ in terms of r_h (equation 26), Σ_0 (equation 21) and $v_c(r_h)$ from equation (38) yields for the phase-space density at the halo radius as

$$Q_{ch} = 7.962\,04\ \frac{I_2(\nu_0)}{[-\xi_h\ \nu'(\xi_h)]^{3/2}} \left(\frac{m}{2\,\mathrm{keV}}\right)^4 \mathrm{keV}^4. \tag{42}$$

The numerical values of Q_{ch} turn to be larger than $Q(0)$ (equation 19) approximately by a factor of 2. In the dilute regime, $M_h \gtrsim 10^6\ \mathrm{M}_\odot$, they are related by

$$Q_{ch} = 2.0873\ Q(0). \tag{43}$$

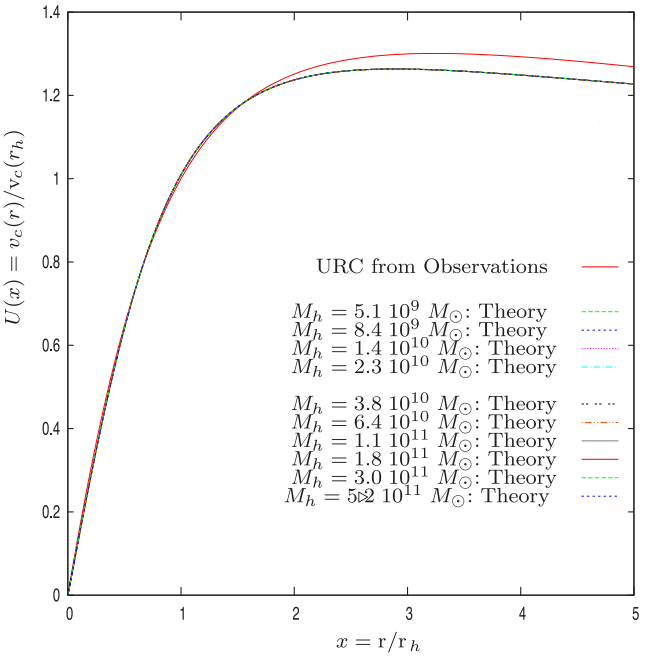

Figure 2. Normalized circular velocities $U(x) = v_c(r)/v_c(r_h)$ versus $x = r/r_h$ from the observational data (equation 46) and from the theoretical Thomas–Fermi formula (equation 38). The theoretical curves from the Thomas–Fermi approach for 10 different galaxy masses all fall one into each other providing aURC which practically coincides with the observational universal curve URC for $x = r/r_h \lesssim 2$.

3 CIRCULAR VELOCITIES CONTRASTED WITH OBSERVATIONS

The circular velocities' values $v_c(r)$ (equation 37) are known with precision from galaxy observational data.

3.1 The galaxy data

The kinematics of about several thousand disc galaxies, described by the rotation curves of spirals, and the information obtained from other tracers of the gravitational field of galaxies, including the dispersion velocities of spheroidals and the weak-lensing measurements (Salucci et al. 2007 and references therein), show that the density of the DM haloes around galaxies of different kinds, different luminosity and Hubble types is well represented, out to the galaxy virial radius, by an empirical Burkert profile

$$\rho_B(r) = \rho_{0\,B}\ F_B\left(\frac{r}{r_{hB}}\right),$$

$$F_B(x) = \frac{1}{(1+x)\ (1+x^2)}\ ,\ x \equiv \frac{r}{r_{hB}}, \tag{44}$$

where ρ_0 stands for the central core density and r_{hB} for the core radius. The empirical Burkert profile satisfactorily fits the astronomical observations and we use the observed data of ρ_{0B} and r_{hB} for DM-dominated spiral galaxies given in Salucci et al. (2007).

Kinematical data and properties of other galaxy gravitational potential tracers are all reproduced, within their observational uncertainty, by a mass model including a DM halo with a Burkert profile (see Salucci et al. 2007; Donato et al. 2009). While some other cored DM distributions [but not the pseudo-isothermal one $\rho_0/(r^2 + a^2)$] may successfully reproduce these data, every cuspy distribution fails to do so (see e. g. Gentile et al. 2004).

The Burkert and the Peñarrubia et al. (2012) profiles are indistinguishable with the data available at present. Any cored density profile with two free parameters (central density, core radius) that decreases faster than $1/r^2$ can be mapped into each other, just by a transformation of the parameters. Only when the determination of the DM density profile will be available at the few per cent error level (today it is 10–30 per cent) we would be able to discriminate between different cored profiles.

The circular velocities $V_{\rm URC,h}(r)$ for the empirical Burkert density profile follow from equations (37) and (44) (Salucci et al. 2007) as

$$V^2_{\rm URC,\,h}(r) = 2\,\pi\,G\,\frac{\rho_{0\,\rm B}\,r^3_{\rm hB}}{r} \times \left[\ln(1+x) - \arctan x + \frac{1}{2}\ln(1+x^2)\right],\ x = \frac{r}{r_{\rm hB}}. \quad (45)$$

Note that normalizing $V_{\rm URC,h}(r)$ to its value at the core radius $r_{\rm hB}$ yields

$$U^2_{\rm URC}(x) \equiv \frac{V^2_{\rm URC,\,h}(r)}{V^2_{\rm URC,\,h}(r_{\rm h})} = \frac{3.932\,01}{x}\left[\ln(1+x) - \arctan x + \frac{1}{2}\ln(1+x^2)\right]. \quad (46)$$

Namely the function $U(x)_{\rm URC}$ only depends on $x = r/r_{\rm hB}$ and complies with the concept of universal rotation curve (URC; Salucci et al. 2007): $U(x)_{\rm URC}$ is an universal function.

Note that the URC concept is valid not only for the Burkert representation of the density profile but also for other density profiles that correctly reproduce the density data.

In the Burkert profile case, the halo galaxy mass follows integrating equation (44) from zero to $r_{\rm hB}$

$$M_{\rm h} = 1.597\,96\ \rho_{0\,\rm B}\ r^3_{\rm hB} = 1.597\,96\ \Sigma_0\ r^2_{\rm hB}\ . \quad (47)$$

This empirical equation can be recasted in a similar form to equation (26) of the theoretical Thomas–Fermi approach as

$$r_{\rm hB} = 72.215\ \sqrt{\frac{120}{\Sigma_0\ {\rm pc}^2}\,\frac{M_{\rm h}}{10^6}}\ \ {\rm pc}. \quad (48)$$

$r_{\rm h}$ in equation (26) and $r_{\rm hB}$ in equation (48) refer to the point where $\rho(r_{\rm h})/\rho(0) = 1/4$ and $\rho_{\rm B}(r_{\rm hB})/\rho(0) = 1/4$ both according to equation (20), for two different density profiles: the theoretical Thomas–Fermi profile $\rho(r)$ in equation (26) and the empirical Burkert profile $\rho(r)_{\rm B}$ for the observational data.

The halo radius $r_{\rm hB}$ and $r_{\rm h}$ for given galaxy mass $M_{\rm h}$ and surface density Σ_0 are related by the universal relation

$$r_{\rm h} = 0.954\,01\ r_{\rm hB},$$

which follows from equations (26) and (47). Namely due to the slight shape difference between the theoretical Thomas–Fermi and empirical Burkert profiles (see Fig. 3), the Thomas–Fermi halo radius turns to be about 5 per cent smaller than the Burkert halo radius.

It follows from equation (14) that the theoretical Thomas–Fermi profile possess an expansion in even powers of r^2 (this is also the case for the density profiles obtained in the linear approximation from the cosmological density fluctuations in de Vega, Salucci & Sanchez 2012a). In contrast, the empirical Burkert profile (equation 44) is not an even function of r and exhibits a linear behaviour in r near the origin. This is the source of the small deviation near $r = 0$ between the theoretical Thomas–Fermi profile and the empirical Burkert profile exhibited in Fig. 3.

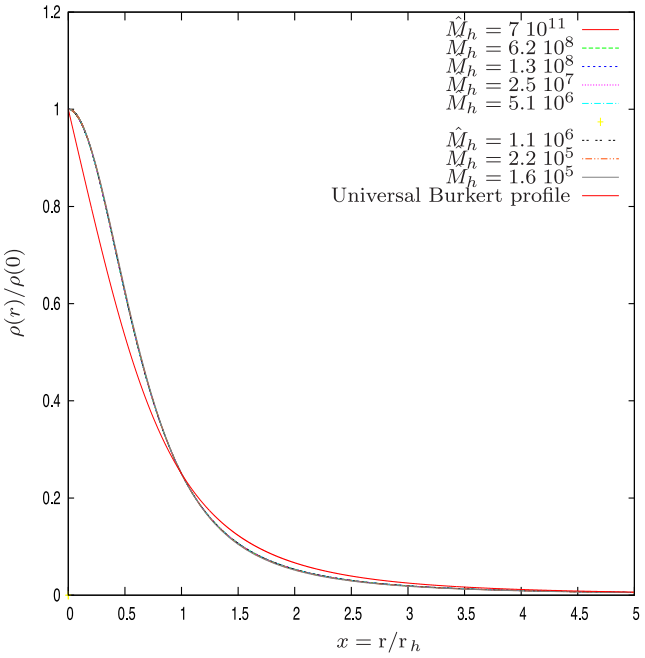

Figure 3. Normalized density profiles $\rho(r)/\rho(0)$ as functions of $r/r_{\rm h}$. We display the theoretical profiles for galaxy masses in the dilute regime $1.4 \times 10^5 < \hat{M}_{\rm h} < 7.5 \times 10^{11}$, $-1.5 > v_0 > -20.78$. All fall into the same and universal density profile. We plot the empirical Burkert profile as function of $r/r_{\rm h}$.

The circular velocity at the halo radius for the empirical Burkert profile follows setting $x = 1$ in equation (45) with the result

$$V_{\rm URC,h}(r_{\rm h}) = 7.717\ \left(\frac{M_{\rm h}}{10^6\ {\rm M}_\odot}\right)^{1/4}\ \left(\frac{\Sigma_0\ {\rm pc}^2}{120\ {\rm M}_\odot}\right)^{1/4}\ \ {\rm km\,s^{-1}}\ .$$

This value is to be compared with the theoretical Thomas–Fermi result (equation 39). We see that they differ from each other by only 2.4 per cent, confirming again the success of the Thomas–Fermi approach to describe the galaxy structures.

3.2 Comparison to observations

Our results are independent of the details of the WDM particle physics model. They follow from the gravitational self-interaction of WDM particles and their fermionic nature. The same remarks apply to all the Thomas–Fermi results including the lower bound $m > 1.91$ keV (DdVS 2013b).

We depict in Fig. 2 the normalized circular velocities $U(x) = v_{\rm c}(r)/v_{\rm c}(r_{\rm h})$ versus $x = r/r_{\rm h}$ obtained on one hand from the observational data $U(x)_{\rm URC}$ described with the empirical Burkert profile (equation 46), and on the other hand, $U(x)$ obtained from the theoretical Thomas–Fermi formula (equation 38). In general, the normalized circular velocities $v_{\rm c}(r)/v_{\rm c}(r_{\rm h})$ can be functions of r and $r_{\rm h}$, which just reflects the fact that in a spherically symmetric approach only one parameter $r_{\rm h}$ shows up in the circular velocities. [The parameter $r_{\rm h}$ depends on the characteristic energy E_0 in the Fermi–Dirac distribution function at fixed surface density Σ_0. Generalizing the Thomas–Fermi approach to non-spherically symmetric and non-isotropic situations by including other particle parameters like the angular momentum in the distribution functions would lead to density profiles depending on other parameters besides $r_{\rm h}$.]

Here, we remarkably find that the normalized circular velocities $v_c(r)/v_c(r_h)$ turn out to be functions of only one variable: the ratio $x = r/r_h$. [On the contrary, $v_c(r)$ is a function of r and r_h separately]. We see that the theoretical curves from the Thomas–Fermi approach for 10 different galaxy masses all fall one into each other. Therefore, we find the result that the Thomas–Fermi approach provides URC. Moreover, the theoretical Thomas–Fermi curves $U(x)$ and the observational universal curve $U(x)_{URC}$ described by the empirical Burkert profile coincide for $r < r_h$.

We depict in Fig. 3 the normalized density profiles $F(x) = \rho(r)/\rho(0)$ as functions of $x = r/r_h$ obtained from the theoretical Thomas–Fermi profiles for galaxy masses in the dilute regime $1.4 \times 10^5 < \hat{M}_h < 7.5 \times 10^{11}$, $-1.5 > \nu_0 > -20.78$. All fall into the same and universal density profile. The empirical Burkert profile $F_B(x)$ in Fig. 3 turns to be very close to the theoretical Thomas–Fermi profile $F(x)$ except near the origin as discussed above.

We display in Fig. 4 $v_c(r)$ in km s^{-1} versus r in kpc obtained on one hand from the observational data described with the empirical Burkert profile (equation 45) and on the other hand from the theoretical Thomas–Fermi formula (equation 38). We plot in Fig. 4 $v_c(r)$ for $0 < r < r_{vir}$, r_{vir} being the virial radius of the galaxy.

The corresponding halo galaxy masses M_h are indicated in Fig. 4 and run from 5.13×10^9 to 5.15×10^{11} M$_\odot$.

The theoretical rotation curves reproduce the observational curves modelized with the empirical Burkert profile for $r \lesssim r_h$ justifying the use of the Fermi–Dirac distribution function (equation 10) in the Thomas–Fermi equations (13) and (14).

We display in Figs 5 and 6 the theoretical density profiles computed from the Thomas–Fermi equations and the observational profiles described by the empirical Burkert expression. We plot the ordinary logarithm of the density in M$_\odot$ pc^{-3} versus r in kpc in the interval $0 < r < 4\ r_h$. We see very good agreement of the theoretical density profiles with the observations modelized with the empirical Burkert profile in all the range $0 < r < 4\ r_h$.

Baryons represent less than 5 per cent of the galaxy mass (Persic et al. 1996; Oh et al. 2008; Memola et al. 2011). For dwarf galaxies, baryons count for less than 0.01 per cent of the galaxy mass (Martin et al. 2008; Woo et al. 2008; Brodie et al. 2011; Willman & Strader 2012; Walker, private communication).

The self-gravity of the baryonic material is negligible while baryons are immersed in a DM halo potential well. Baryons trace the DM potential well playing the role of test particles to measure the local DM density.

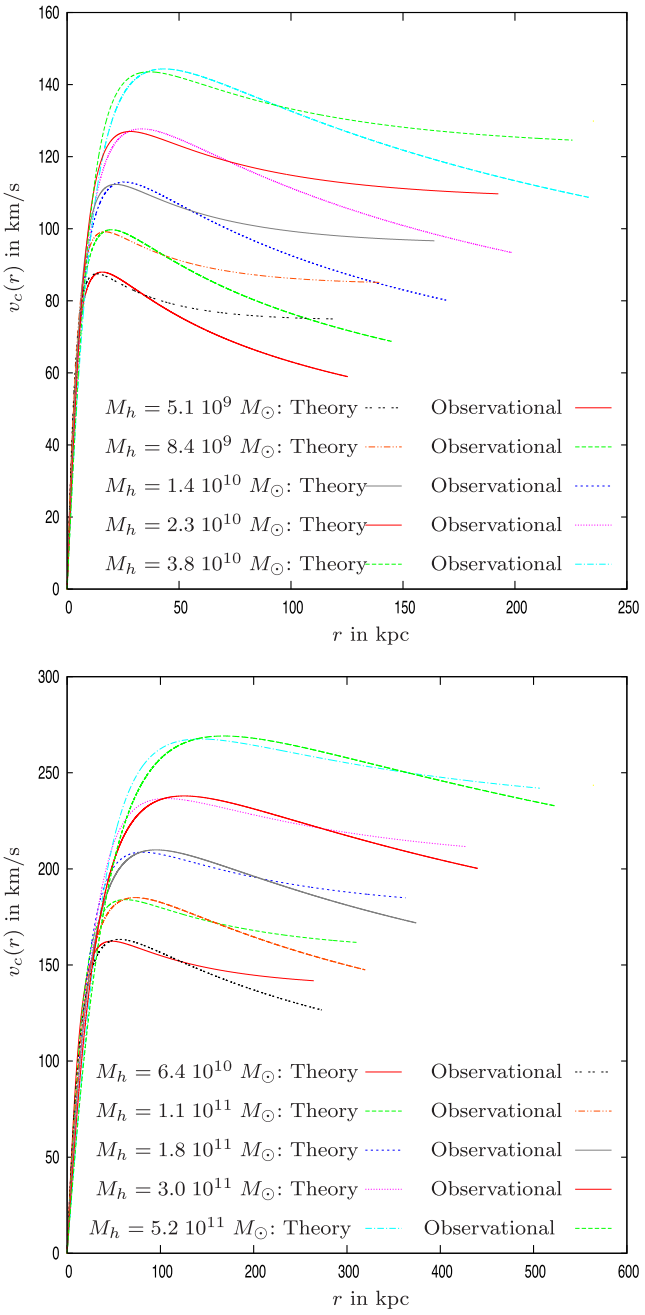

Figure 4. The velocity rotation curves $v_c(r)$ in km s^{-1} versus r in kpc for 10 different independent galaxy masses M_h going from 5.13×10^9 to 5.15×10^{11} M$_\odot$. For each galaxy mass M_h, we show the two curves: the theoretical Thomas–Fermi curve and the observational curve described by the empirical Burkert profile. The Thomas–Fermi curves reproduce remarkably well the observational curves for $r \lesssim r_h$. We plot $v_c(r)$ for $0 < r < r_{vir}$, r_{vir} being the virial radius of the galaxy.

4 CONCLUSIONS

The more appropriate way to decipher the nature of the DM is to study the properties of the physical objects formed by it: galaxies are formed overwhelmingly by DM since 95 to 99.99 per cent of their mass is dark. This is the task we pursue in this paper.

Fermionic WDM by itself produce galaxies and structures in agreement with observations modelized with the empirical Burkert profile showing that baryonic corrections to WDM are not very important. Therefore, the effect of including baryons is expected to be a correction to the pure WDM results, consistent with the fact that DM is in average six times more abundant than baryons.

The theoretical curves from the Thomas–Fermi approach to galaxy structure for self-gravitating fermionic WDM (DdVS 2013a,b) practically coincide with the observed galaxy rotation curves and density profiles described with the empirical Burkert profile for $r < 2\ r_h$. In addition, our approach provides scaling relations for the main galaxy magnitudes (equations 26–31) as the halo radius r_h, mass M_h and phase-space density.

Therefore, the Fermi–Dirac distribution applies in the region $r \lesssim 2\ r_h$ for the whole range of galaxy masses.

Note that the scaling relations (equations 26–31) are a consequence solely of the self-gravitating interaction of the fermionic WDM.

The galaxy relations derived in equations (26)–(31) are accurate for $M_h \gtrsim 10^6$ M$_\odot$. We see that they exhibit a scaling behaviour

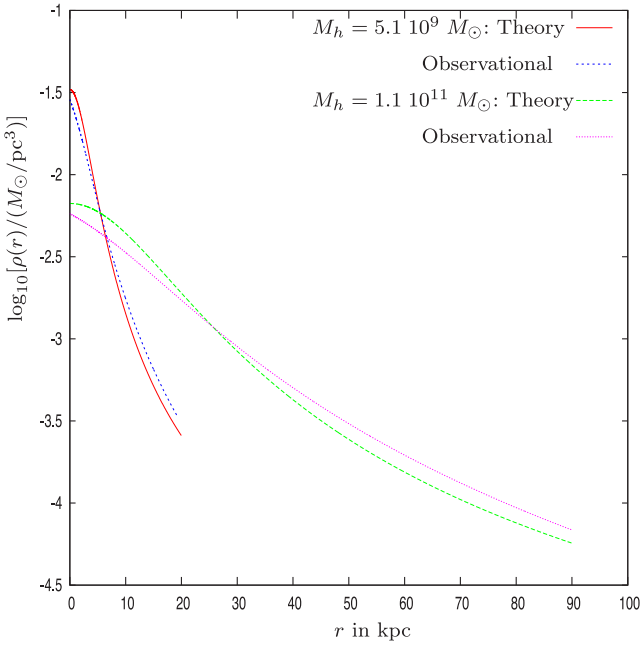

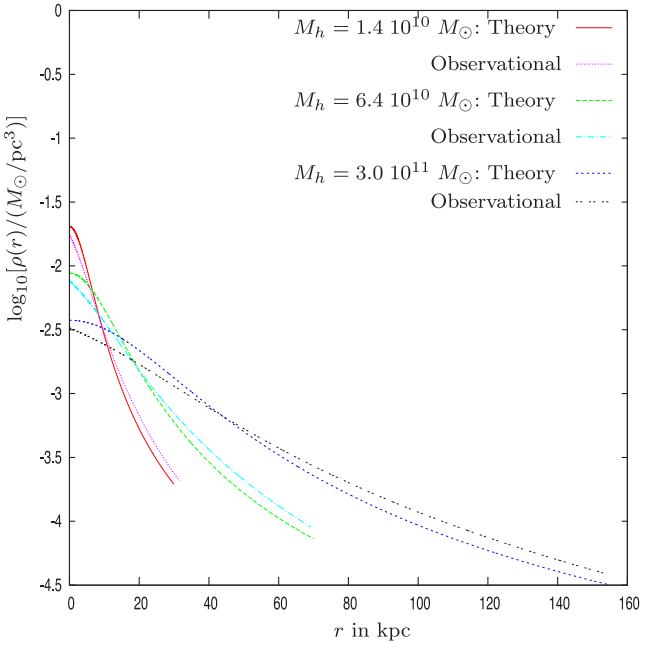

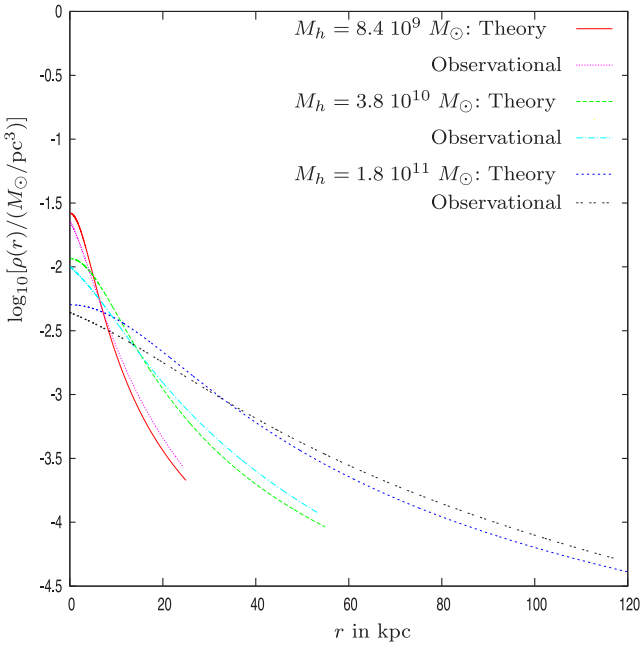

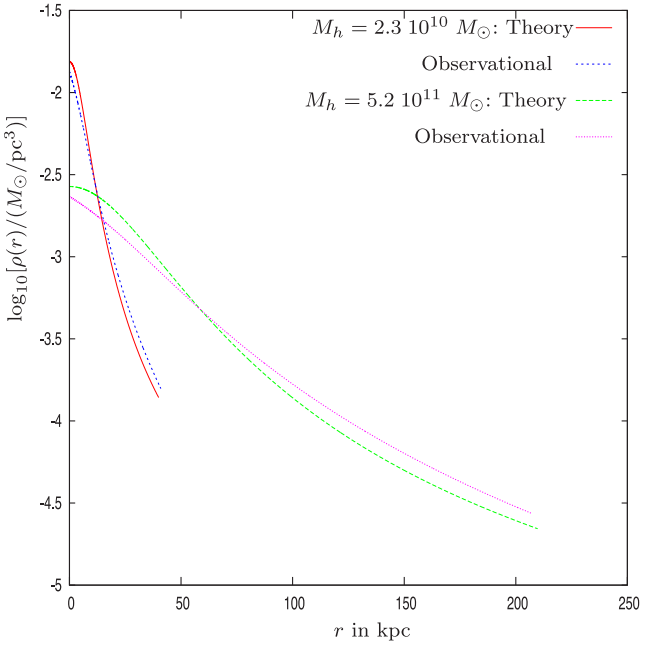

Figure 5. The theoretical Thomas–Fermi density profiles and the observational profiles described by the Burkert expression for the first five galaxy masses. We plot the ordinary logarithm of the density in $\mathrm{M}_\odot\,\mathrm{pc}^{-3}$ versus r in kpc in the interval $0 < r < 4\ r_\mathrm{h}$. For each galaxy mass M_h, we show the two curves: the theoretical Thomas–Fermi curve and the observational Burkert curve. The agreement of the Thomas–Fermi curves to the observational curves is remarkable.

Figure 6. The theoretical Thomas–Fermi density profiles and the observational profiles described by the Burkert expression for further five galaxy masses. We plot the ordinary logarithm of the density in $\mathrm{M}_\odot\,\mathrm{pc}^{-3}$ versus r in kpc in the interval $0 < r < 4\ r_\mathrm{h}$. For each galaxy mass M_h, we show the two curves: the theoretical Thomas–Fermi curve and the observational Burkert curve. The agreement of the Thomas–Fermi curves to the observational curves is remarkable.

for r_h versus M_h, $Q(0)$ versus M_h and M_h versus the fugacity at the centre $z_0 = \mathrm{e}^{\mu(0)/E_0}$. These scaling behaviours of the dilute classical regime are very accurate even near the degenerate limit as shown by Fig. 1. Interestingly enough, the small deviation of these scaling laws near the degenerate limit is a manifestation of the quantum effects present in compact dwarf galaxies.

The theoretical circular velocities $v_\mathrm{c}(r)$ and the theoretical density profiles $\rho(r)$ computed from the Thomas–Fermi equation (6) reproduce very well the observational curves modelized with the empirical Burkert profile for $r \lesssim r_\mathrm{h}$ as shown in Figs 3–6. These results fully justify the use of the Fermi–Dirac distribution function in the Thomas–Fermi equation (6).

Remarkably enough, solving the Thomas–Fermiequation (6) we find that the theoretical circular velocities $U(x) = v_\mathrm{c}(r)/v_\mathrm{c}(r_\mathrm{h})$ as well as the normalized density profiles $F(x) = \rho(r)/\rho(0)$ are only functions of $x = r/r_\mathrm{h}$ and take, respectively, the same value for all galaxy masses in the range going from 5.13×10^9 to

$5.15 \times 10^{11}\,M_{\odot}$ as shown in Figs 2 and 3. Namely the Thomas–Fermi approach provides universal functions $U(x)$ and $F(x)$ for the normalized circular velocities and normalized density profiles, respectively. Moreover, Figs 2 and 3 show that the observational universal curves and the theoretical Thomas–Fermi curves coincide for $r \lesssim 2\,r_{\rm h}$.

These important results show the ability of the Thomas–Fermi approach to correctly describe the galaxy structures.

ACKNOWLEDGEMENTS

PS thanks the Observatoire de Paris LERMA and the CIAS for their kind invitation and hospitality.

REFERENCES

Anderhalden D., Schneider A., Macciò A. V., Diemand J., Bertone G., 2013, J. Cosmol. Astropart. Phys., 03, 014
Avila-Reese V., Colín P., Valenzuela O., D'Onghia E., Firmani C., 2001, ApJ, 559, 516
Biermann P. L., de Vega H. J., Sanchez N. G., 2012, preprint (arXiv:1305.7452)
Brodie J. P., Romanowsky A. J., Strader J., Forbes D. A., 2011, AJ, 142, 199
Colín P., Valenzuela O., Avila-Reese V., 2000, ApJ, 542, 622
Colín P., Valenzuela O., Avila-Reese V., 2008, ApJ, 673, 203
de Vega H. J., Sanchez N. G., 2013, preprint (arXiv:1304.0759)
de Vega H. J., Salucci P., Sanchez N. G., 2012a, New Astron., 17, 653
de Vega H. J., Falvella M. C., Sanchez N. G., 2012b, preprint (arXiv:1307.1847)
Destri C., de Vega H. J., Sanchez N. G., 2013a, New Astron., 22, 39 (DdVS 2013a)
Destri C., de Vega H. J., Sanchez N. G., 2013b, Astropart. Phys., 46, 14 (DdVS 2013b)
Destri C., de Vega H. J., Sanchez N. G., 2013c, Phys. Rev. D, 88, 083512
Donato F. et al., 2009, MNRAS, 397, 1169
Gao L., Theuns T., 2007, Science, 317, 1527
Gentile G., Salucci P., Klein U., Vergani D., Kalberla P., 2004, MNRAS, 351, 903
Kormendy J., Freeman K. C., 2004, in Ryder S. D., Pisano D. J., Walker M. A., Freeman K. C., eds, Proc. IAU Symp. 220, Dark Matter in Galaxies. Astron. Soc. Pac., San Francisco, p. 377
Landau L. D., Lifshits E. M., 1980, Statistical Mechanics. Elsevier, Oxford
Lovell M. R. et al., 2012, MNRAS, 420, 2318
Lovell M. R., Frenk C. S., Eke V. R., Jenkins A., Gao L., Theuns T., 2014, MNRAS, 439, 300
Macciò A., Paduroiu S., Anderhalden D., Schneider A., Moore B., 2012, MNRAS, 424, 1105
Martin N. F., de Jong J. T. A., Rix H.-W., 2008, ApJ, 684, 1075
Memola E., Salucci P., Babić A., 2011, A&A, 534, A50
Menci N., Fiore F., Lamastra A., 2013, ApJ, 766, 110
Merle A., 2013, Int. J. Mod. Phys. D, 22, 1330020
Nierenberg A. M., Treu T., Menci N., Lu Y., Wang W., 2013, ApJ, 772, 146
Oh S. H., de Blok W. J. G., Walter F., Brinks E., Kennicutt R. C., Jr, 2008, AJ, 136, 2761
Pacucci F., Mesinger A., Haiman Z., 2013, MNRAS, 435, L53
Papastergis E., Martin A. M., Giovanelli R., Haynes M. P., 2011, ApJ, 739, 38
Peñarrubia J., Pontzen A., Walker M., Koposov S., 2012, ApJ, 759, L42
Persic M., Salucci P., Stel F., 1996, MNRAS, 281, 27
Salucci P., Lapi A., Tonini C., Gentile G., Yegorova I., Klein U., 2007, MNRAS, 378, 41
Sommer-Larsen J., Dolgov A., 2001, ApJ, 551, 608
Spano M., Marcelin M., Amram P., Carignan C., Epinat B., Hernandez O., 2008, MNRAS, 383, 297
Tikhonov A. V., Gottlöber S., Yepes G., Hoffman Y., 2009, MNRAS, 399, 1611
Tonini C., Lapi A., Shankar F., Salucci P., 2006, ApJ, 638, 13
Tremaine S., Gunn J. E., 1979, Phys. Rev. Lett., 42, 407
Viel M., Becker G. D., Bolton J. S., Haehnelt M. G., 2013, Phys. Rev. D, 88, 043502
Viñas J., Salvador-Solé E., Manrique A., 2012, MNRAS, 424, L6
Watson C. R., Li Z., Polley N. K., 2012, J. Cosmol. Astropart. Phys., 03, 018
Willman B., Strader J., 2012, AJ, 144, 76
Woo J., Courteau S., Dekel A., 2008, MNRAS, 390, 1453
Zavala J., Jing Y. P., Faltenbacher A., Yepes G., Hoffman Y., Gottlööber S., Catinella B., 2009, ApJ, 700, 1779

This paper has been typeset from a TEX/LATEX file prepared by the author.